Securable Networks for Nonintrusive Sensor Fusion

Aaron W. Langham, *Graduate Student Member, IEEE*, Andrew Moeller, Devin W. Quinn,
Thomas C. Krause, *Graduate Student Member, IEEE*, Daisy H. Green, *Member, IEEE*,
and Steven B. Leeb, *Fellow, IEEE*

***Abstract*—Fault detection and diagnostics (FDD) and energy scorekeeping for power systems can be performed nonintrusively with current and voltage sensing at a utility panel. The key problem remains that some important electromechanical behavior, including vibration and acoustic signatures, cannot be easily detected in the power stream, and a small set of additional sensors may be necessary for automated analysis. A nonintrusive power monitor can serve as a central point for collating or "fusing" sensor data from remote sensors, providing a correlated picture of remote sensor data with power consumption. A local, physically secured intranet eases the cybersecurity challenge of a facility by avoiding conventional Internet of Things (IoT) solutions. This article demonstrates a Wi-Fi-based implementation of an FDD intranet on the microgrids of several marine vessels. Connectivity tests presented in this work show that Wi-Fi is a viable link medium for an FDD intranet in shipboard environments. In addition, this work demonstrates the ability to track pump pressure, air conditioning (A/C) compressor loading state, and fan imbalance using fused nonintrusive sensing. Cyclostationary signal processing techniques identified a faulty relief valve in a vacuum pump that evaded traditional analysis. Four sensor network strategies are presented for these scenarios. This work concludes that synchronized power and vibration data provide complementary fault detection ability.**

***Index Terms*—Fault detection, power monitoring, sensor fusion, vibration analysis, wireless networks.**

I. INTRODUCTION

INTERNET of things (IoT) solutions have pervaded consumer and industrial markets, proliferating the application of computing and sensing for measurement and maintenance [1], [2], [3]. Networking solutions that rely on an external or third-party server expose communications to interception and security risks. These solutions also generally fail to collate and correlate sensor data to provide actionable information without resorting to additional networked processing, further exposing potentially sensitive information and conclusions. The Internet client–server model has created an "arms race" of authentication and encryption in an attempt to secure data and decisions. This arms race is frequently a losing battle. There is another way.

For many industrial facilities and transportation systems, a self-contained client–server model can be physically secured at the target site. That is, physical access to data and processed information can be denied, even to trusted participants, who are not physically and verifiably proximate to the system and data. Computing power has reached a point where local systems are able to provide scientific computing without resorting to external computing devices. Even machine learning algorithms with computationally expensive training can produce systems that can evaluate inputs quickly and efficiently [4]. When adaptation for machine learning systems can be provided over reasonable time periods, local computing may be entirely satisfactory for fault detection and diagnostics (FDD) in a mission-critical facility.

For instrumentation and measurement challenges, a client–server model provides the convenience of a server that can collate data from a set of sensor node "clients." For FDD applications for electromechanical systems, a nonintrusive load monitor (NILM) is in many ways an ideal "server" for coordinating data exchange and analysis. On its own, a NILM uses a single or limited set of voltage and current sensors to monitor the power consumption of electrical loads downstream of the metered point [5]. State-of-the-art NILM techniques enable individual load identification using machine learning and signal processing techniques [6]. Nonintrusive load monitoring has been demonstrated extensively for residential energy disaggregation [7], [8]. In addition, NILMs installed in industrial settings can perform automatic logging and watchstanding with knowledge of load operation and timing [9]. Industrial NILMs have been demonstrated to identify "soft" faults and presage impending "hard" faults that produce equipment failure by recognizing evolving power signatures for individual loads [10].

However, a challenge in industrial FDD with a NILM is that electrical power data are not always sufficient to diagnose certain faults. Additional measurements, such as vibration, temperature, and acoustic signatures, are required in these scenarios to reveal diagnostic indicators absent in the electrical data. A NILM can then correlate these measurements with the corresponding electrical events. Design requirements and challenges for FDD in an industrial setting through sensor fusion include the ability to securely collate sensor data without collecting more high-bandwidth data than necessary. An "FDD intranet" operated by the NILM facilitates this exchange and fusion of sensor data for FDD analysis. This triggered data collection alleviates unnecessary data storage and also provides physical correlation between data streams for FDD analysis. The NILM is an ideal device

---

Manuscript received 13 September 2022; revised 17 November 2022; accepted 3 December 2022. Date of publication 19 December 2022; date of current version 11 January 2023. This work was supported in part by the Office of Naval Research NEPTUNE Program and in part by The Grainger Foundation. The Associate Editor coordinating the review process was Dr. Shibin Wang. *(Corresponding author: Aaron W. Langham.)*

Aaron W. Langham, Andrew Moeller, Devin W. Quinn, Thomas C. Krause, and Steven B. Leeb are with the Department of Electrical Engineering and Computer Science (EECS), Massachusetts Institute of Technology, Cambridge, MA 02139 USA (e-mail: alangham@mit.edu).

Daisy H. Green is with the Department of Architecture, Massachusetts Institute of Technology, Cambridge, MA 02139 USA.

Digital Object Identifier 10.1109/TIM.2022.3230467

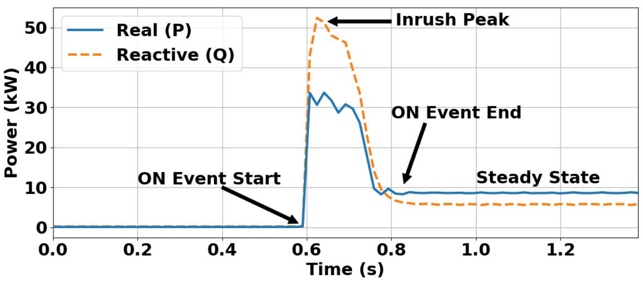

Fig. 1. CPP pump turn-on power transient acquired by a NILM.

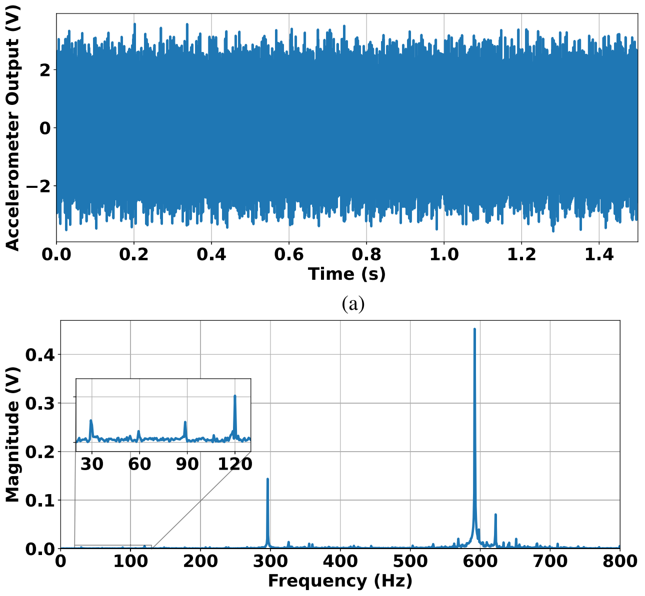

(a)

(b)

Fig. 2. CPP pump steady-state vibration signature in (a) time and (b) frequency domains.

for interacting with watchstanders or maintainers, as it can provide analysis and reports for addressing impending FDD problems before they become mission failures. Communication outside the facility is still possible, e.g., over the Internet. However, these communications can involve only the level of detail and analysis considered to be both useful and secure. Perhaps most importantly, the FDD intranet can be physically secured to provide detailed information and analysis only to trusted operators physically present in a facility or system.

This article demonstrates a new, wireless-enabled NILM implementation that coordinates both power monitoring and data retrieval from distributed vibration sensors. Wireless networks are configured using the custom NILM hardware to create shipboard diagnostic monitors that can only be accessed from inside the facility. The utility of the wireless intranet and multiple-sensor fault detection case studies are demonstrated with shipboard measurements taken on several U.S. Coast Guard Cutters (USCGCs).

II. SENSOR HARDWARE

A NILM senses the voltage and current signals at a single point in a power system. The current and voltage waveforms are sampled (in this work at 8 kHz). A spectral envelope preprocessor is run using the digitized current and voltage waveforms [11], producing a stream of aggregate real power, reactive power, and higher harmonic current consumption sampled at the utility frequency (60 Hz). A turn-on transient of both real and reactive fundamental power of an electromechanical load is shown in Fig. 1. A continuously running event detector identifies transient events, from which features such as inrush and steady-state power are extracted [6]. Using these features, the NILM classifies events to individual loads and identifies faulty behavior. Abrupt faults such as an open-circuited heating element are immediately obvious in the power stream [12]. Gradual variations in load power consumption over time can be tracked to identify "soft faults" that may eventually cause complete load failure. Finally, from the sequence of load events, the NILM can diagnose timing faults and errant duty cycles [13].

However, a pervasive challenge in the NILM-based FDD is that many critical diagnostic measurements cannot be derived from the power stream. These include, but are not limited to, vibration, acoustic, and temperature data. Augmentation of nonintrusive power monitoring with sensor data such as light level and acoustics has been proposed and evaluated for load identification and energy estimation, which are common NILM applications [14], [15]. Fusion schemes of features such as submetered (rather than aggregate) current, acoustic, and vibration data have been demonstrated for diagnosing faults in induction motors [16], [17]. Sensor fusion theory encompasses several techniques to handle multiple sources of imperfect data. Some examples include Kalman filtering, Dempster–Schafer theory, and convolutional neural networks [18], [19]. However, in the interest of simplicity, this work uses heuristic-based techniques such as spectrum analysis. The fault and condition change detection discussed in this work could be extended to incorporate these techniques if desired.

As a case study to illustrate how sensor fusion can reveal electromechanical operation, consider the load in Fig. 1. This load is a controllable pitch propeller (CPP) pump in the engine room of a U.S. Coast Guard Cutter (USCGC), which provides hydraulic pressure for changing the pitch of the ship's propeller. Aggregate power data show recognizable turn-on transients, which the NILM can use to track load operational status. Fig. 2 shows vibration data in both the time and frequency domains captured during steady-state load operation. At rated load, an induction machine drives the hydraulic gear pump at 1725 rpm. The shaft rotation creates peaks in the vibration frequency-domain plot at multiples of a little less than 30 Hz. Pump gear teeth meshing likely produces the large peaks located slightly below 300 and 600 Hz, multiples of the shaft frequency [20], [21]. These indicators are entirely absent in the power stream and provide insight on the physical load behavior. Fig. 3 shows acoustic data from this load while the propeller's pitch was modified, as indicated by the envelope of the signal. Steady-state signatures and spontaneous changes in operation are difficult to diagnose in aggregate power data, since the source of the behavior is inherently

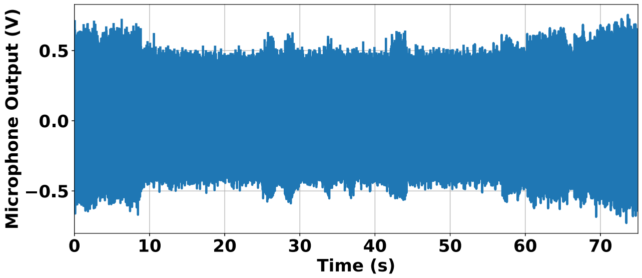

Fig. 3. CPP pump acoustic signature during changing propeller pitch.

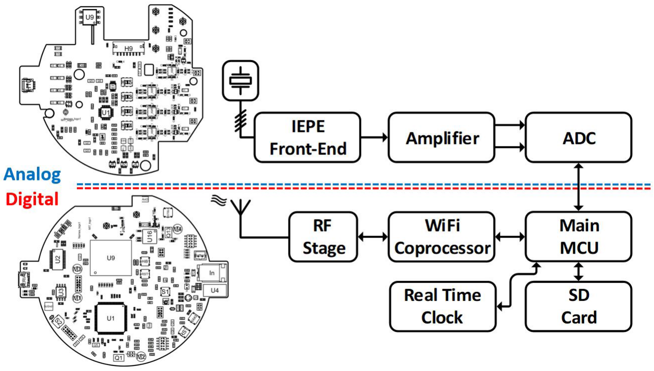

Fig. 4. Block diagram of the wireless sensor platform of [23].

uncertain. These sensor data sources are thus complementary, and all the three show a different and interesting side of the machine's operation.

To measure these quantities and supplement the NILM's power measurements, the sensor platform described in [22] and [23] serves as an easily installable distal sensor node. A block diagram of this device is shown in Fig. 4. The sensor platform acquires signals from up to four channels and supports sampling rates up to 128 kHz with 16- or 24-bit resolution. Each acquisition channel can measure arbitrary +/−5-V signals or signals from integrated electronics piezoelectric (IEPE) sensors. The IEPE standard provides high noise immunity and power and signal delivery on the same two wires. Since the IEPE interface is limited to ac signal transmission, the companion hardware proposed in [23] extends IEPE to include dc and slowly varying quantities. The IEPE channels on the sensor platform can interface with any resistive or voltage-based sensor such as thermistors, strain gauges, and pressure sensors, as well as traditional IEPE devices such as microphones and accelerometers. The diverse set of compatible sensing elements provides a unique opportunity for diagnostics that complement electrical data observed by the NILM. Vibration analysis is particularly useful for electromechanical load diagnostics, as changes in mechanical health are often reflected in the vibration signature of the machine [22], [24].

The challenge that remains is that unless sensors are interlinked, tandem electromechanical diagnostic information is limited to being offline and *post hoc*. Without synchronized and colocated data, there will be an inevitable delay between physically measurable indications of a fault and the actionable information for a watchstander to fix the fault. However, an intranet of sensors for FDD provides the ability to fuse sensor data and perform predictive, online analysis. Using a dashboard for human–computer interaction [9], the NILM makes this information actionable to watchstanders who can actually fix the fault as it happens. The novelty of this work is the demonstration of an enhanced NILM that can host a physically securable FDD intranet using wired or wireless channels for collating data from remote sensor nodes. Fig. 5 shows the upgraded NILM implementation capable of creating a Wi-Fi intranet and functioning as the server for the sensing network. Table I outlines a comparison of this new NILM implementation with previous implementations. Where necessary and desired, sensor nodes such as the one shown in Fig. 5 (right) are located remote from the NILM but in Wi-Fi communication range. Fig. 6 shows a block diagram of the system. Our experiments with this system use a commercial, off-the-shelf Wi-Fi router in the NILM to cover the key areas of a monitored space. Two 5-dBi Wi-Fi antennas mounted to the case provide spatial diversity to combat multipath fading from environments adverse to Wi-Fi transmission [25]. Broadcast power is limited so that usable signal strength is empirically verified to extend no farther than the desired internal secure areas on the ship. Although ships are used as a case study in this work, the proposed sensor network can be deployed to any number of systems. The key limitations are that a NILM is installed, a set of interesting loads and corresponding sensor types are identified, and a common channel for communication (e.g., Ethernet or Wi-Fi) is available.

Fig. 5. Wi-Fi-enabled NILM alongside the wireless sensor platform.

TABLE I

COMPARISON OF THIS WORK'S CONTRIBUTION AND PREVIOUS NILM IMPLEMENTATIONS

	Previous NILM	Wi-Fi-Enabled NILM
Measurements	Electrical power only	Electrical power + vibration, acoustic, temperature, etc.
Multisensor analysis	Offline, *post-hoc*	Online, real-time
Identical loads	Cannot be distinguished	Can be distinguished with remote sensor data

III. PHYSICALLY SECURED NETWORK

The NILM can use either wired or wireless channels for creating a secured sensor network. However, wireless

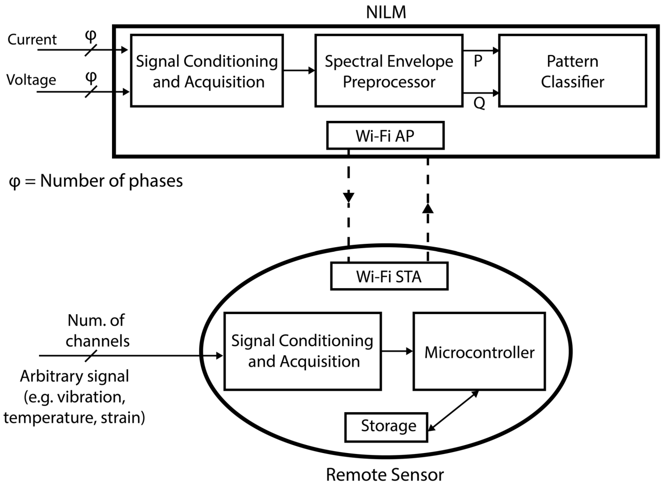

Fig. 6. Block diagram of the NILM and wireless sensor platform operation.

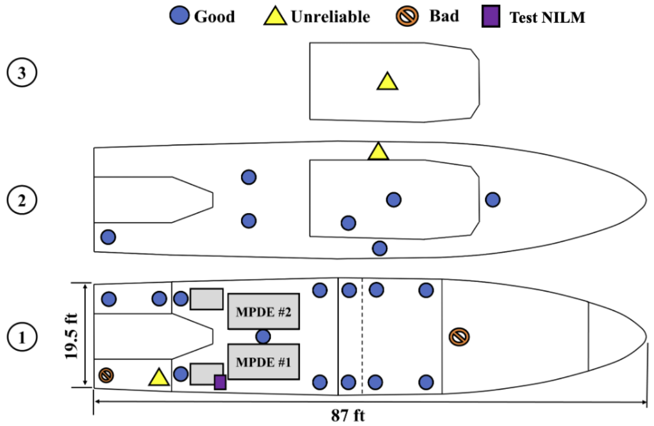

Fig. 7. Connectivity test results for USCGC MARLIN. The test NILM is shown with a purple rectangle, and the gray shapes show large shipboard equipment such as the MPDEs.

configurations allow for minimally invasive and easily changeable sensing solutions. Although many other wireless technologies exist, including Bluetooth and Zigbee, this work uses Wi-Fi as a link medium that is securable through encryption and can be implemented inexpensively with commercial, off-the-shelf hardware. To evaluate wireless transmission, point-to-point radio communication can be modeled with the Friis transmission model [26]. The received power can thus be calculated if the transmitting and receiving antenna gains, path distance, transmission frequency, and transmission power are known. However, this model does not include multipath effects, in which reflections cause a transmission to arrive along many paths with varying delays. These effects may be random and time-varying and are prevalent in industrial environments [27]. Therefore, in addition to being limited by distance and broadcast strength, wireless communication is often assumed to be ill-suited in industrial and shipboard environments [27], [28], [29], [30]. Rather than create intricate transmission models, we evaluated the performance of Wi-Fi in shipboard environments empirically. Our experiments show that Wi-Fi is a viable communication channel for shipboard FDD with multiple sensors.

A. Wi-Fi Evaluation

Wi-Fi was evaluated as a candidate channel for the FDD intranet aboard three USCGCs of various sizes and construction types. Connectivity was tested using the new wireless-enabled NILM (referred to as the "test NILM") and remote sensor platform of Section II. In each connectivity test, the test NILM was placed near the utility panels to emulate a real installation. The test NILM created a Wi-Fi access point (AP), and the sensor platform connected to this AP as a client. Thus, the location of the AP was fixed during the test, such that the AP was located next to the utility panel. Evaluating the connection strength between the test NILM and the sensor platform as it was moved about a lattice of test points produced a "heatmap" of Wi-Fi connectivity for each environment.

The test NILM was used to run the following four tests for wireless connectivity: 1) maintain a Wi-Fi connection throughout testing without dropping packets, evaluated using the `ping` utility; 2) access the sensing device's memory and list all the files in storage; 3) direct the sensing device to capture a sample measurement of data; and 4) successfully download the sample measurement from the sensing device to the test NILM. Test points are labeled as "good" if they passed all the four tests. Test points that passed one to three of these tests are labeled as "unreliable." Test points that could not support a Wi-Fi connection are labeled "bad."

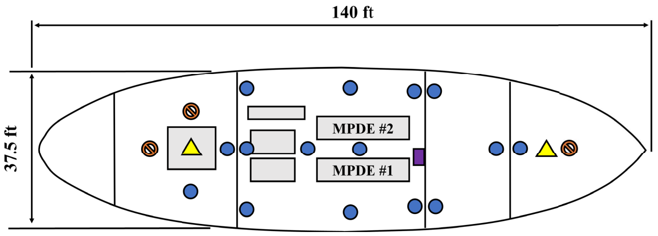

Fig. 8. Connectivity test results for USCGC THUNDER BAY.

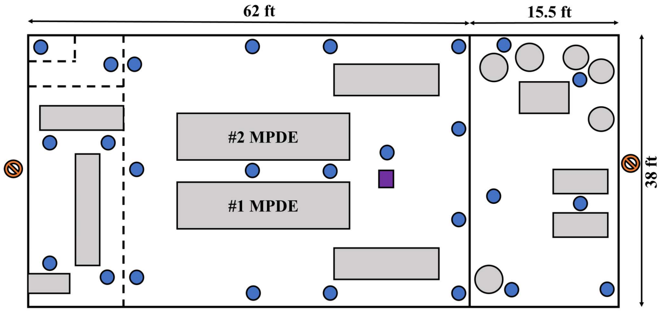

Fig. 9. Connectivity test results in the upper engine room for USCGC SPENCER.

Figs. 7–10 show the heatmaps generated from the wireless tests conducted in the three shipboard environments. The "good" tests are represented by blue dots, the "unreliable" tests are represented by yellow triangles, and the "bad" tests are represented by orange slashed circles. Solid lines represent airtight and watertight bulkheads that span the entire width

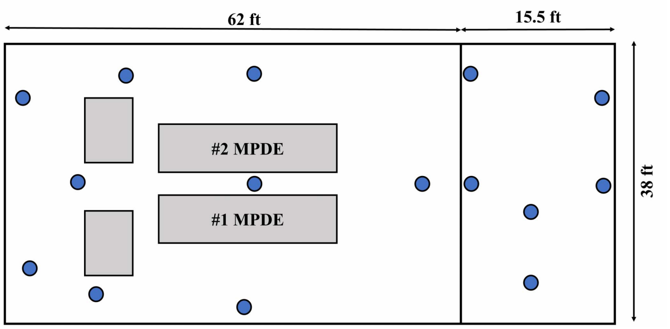

Fig. 10. Connectivity test results in the lower engine room for USCGC SPENCER.

of the ship. Dashed lines denote bulkheads that are neither airtight nor watertight. Finally, the purple rectangle represents the location of the test NILM. Gray shapes indicate other significant equipment and obstructions such as main propulsion diesel engines (MPDEs), electrical generation equipment, and holding tanks.

The first of the three shipboard environments tested was USCGC MARLIN, a 87-ft coastal patrol boat. Fig. 7 shows the testing results on three levels of the ship. The wireless range was sufficient to link almost all the test points on the second level with the test NILM located on the first level. The second environment was USCGC THUNDER BAY, a 140-ft icebreaking tug. As shown in Fig. 8, there was a strong wireless connection throughout the entire engine room. In addition, the wireless connection was able to reach through the forward transverse bulkhead into the auxiliary machinery room. The final environment was USCGC SPENCER, a 270-ft medium endurance cutter. Figs. 9 and 10 show the testing results for the upper and lower engine rooms, respectively. Both the spaces supported a Wi-Fi connection between the test NILM and the sensor platform. Each shipboard environment showed that Wi-Fi proved to be stable and reliable for the majority of the regions containing electromechanical loads of interest.

B. Data Transmission and Synthesis

Once a communication channel is acquired via Wi-Fi, either the NILM or the sensor platform initiates data transmission, depending on the use case. Choice of network protocol is an important design consideration, with the two prominent choices being the transmission control protocol (TCP) and user datagram protocol (UDP). For certain IoT and cyber-physical applications, UDP is attractive, since it prioritizes speed and simplicity in packet transmission, at the expense of reliability [3]. However, TCP is more suitable for the FDD intranet, since it guarantees reliability. The additional power and computation overhead of establishing a connection and verifying data integrity is more than outweighed by the assurance that data are received in order. This is especially significant for automatic FDD, because a corrupted data transmission may cause a critical sensor measurement to be missed entirely. Using separate TCP ports and sockets for each remote sensor node, conflicts in sending and processing data can be avoided.

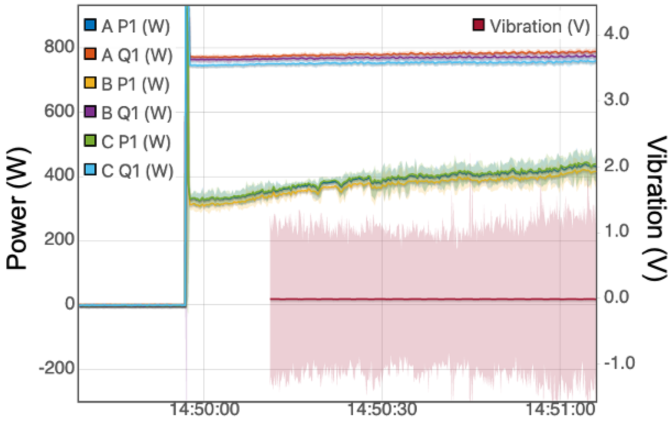

Fig. 11. Power and vibration data streams, captured synchronously with multiple sensors.

Data are processed with Joule [31], which models the data pipelines as a series of “modules” with streams of information passing between them, allowing for efficient, real-time measurement and signal processing. Joule modules are used to continuously run an event detector, feature extractor, and classifier on the power stream to identify load transient events. Once a load event is found, a separate Joule module establishes a TCP/IP socket with the wireless sensor platform of interest. The sensor takes a measurement for a user-configured duration and then sends the data back through the socket. Since timestamps from the remote sensor nodes are not guaranteed to be available or reliable, the NILM infers them to avoid clock drift and time misalignment. This is done via linear interpolation when data of a known duration are retrieved. Once data are received and timestamped, they are inserted into a time-series database [5] for further analysis.

A case study is shown here for a reciprocating air conditioning (A/C) compressor. The NILM is configured to direct the sensor platform to capture 2 min of vibration data whenever the NILM detects a transient event in the power stream. Fig. 11 shows the resulting synchronized and colocated data from both power and vibration sensors, plotted with the Lumen data visualization app on the NILM [32]. Real and reactive fundamental power are plotted on the left axis for all the three phases. Vibration is plotted on the right axis in red; due to the decimation performed by the data visualizer [5], the solid red line shows the average value (zero) and the lighter red region shows the envelope of the accelerometer measurements. With access to both these data streams, the NILM can perform online analysis and provide actionable information for load diagnostics in real-time.

C. Security

Strong, unbroken encryption is the keystone of modern network security. As such, the FDD network provides both encryption and authentication of network members using Wi-Fi Protected Access II (WPA2). However, the FDD network provides two additional security layers. First, the network is intentionally isolated from the public Internet, in contrast to the IoT strategy. This “air-gapped” scheme denies many attack vectors into the system by simply making it inaccessible to public channels. However, this shifts some of the security burden onto the process of moving data to and from the network. Care must be taken that any interactions with external computers, such as Internet connection and removable media, are trusted.

Second, many environments relevant to FDD, such as ships, naturally attenuate wireless signal power at their boundaries. Carefully adjusting broadcast power of the NILM's AP to what is only necessary limits the network signals' ability to reach the outside world. As an example, consider the shipboard environments presented previously. The wireless signals broadcast from the two devices' radios permeate the bulkheads and hull of the ship only minimally, since the ship's steel hull acts as a Faraday cage that blocks the electromagnetic fields. For a ship on open water, it would be difficult for an adversary to be in reception range without detection, without immensely powerful radio equipment. Finally, it is worth emphasizing again that these two additional layers do *not* take the place of up-to-date encryption and authentication practices, as a sufficiently determined and powerful adversary may find a way to communicate with the network.

D. Sensor Placement

When deploying a nonintrusive sensor network, there exists a trade-off between maintaining a low sensor count and obtaining actionable diagnostic information. The appropriate number of sensors is ultimately subject to the interests of the system operator. As a general guideline, however, loads that are known to contain behavior invisible in the power stream should be identified. Remote nodes with the appropriate sensor can then be installed and connected to the NILM. If the rest of the electromechanical behavior of interest can be identified by the NILM, this provides a reasonable balance of low sensor count and access to diagnostic information.

IV. SENSOR DEMONSTRATION

This section provides four case study scenarios in which fused nonintrusive sensor data streams are used in tandem to shed further light on load operation and diagnostics than power data alone provide. Centralized sensor fusion is achieved by first collating data on the NILM from multiple sensors (in these examples, power and vibration), and then generating diagnostic indicators from the sensor data streams. Scenarios A and B (in Sections IV-A and IV-B) show a condition change apparent in the electrical power stream, and thus can be detected with a NILM implementation without remote sensors, although imperfectly. Condition changes in large machinery often do not create usable indicators in electrical power data [22], [33]. In addition, these indicators may be very small in remote sensor data such as vibration. Signal processing techniques that exploit the physical structure of the mechanical process can recover these small signals [34]. As confirmation, scenarios C and D (in Sections IV-C and IV-D) show examples of these condition changes that are invisible to a NILM implementation without remote sensing, and the use of vibration analysis, including cyclostationary signal processing, to detect them. Each of these four scenarios corresponds to a separate FDD network strategy for collating the sensor data and generating diagnostic indicators. These FDD network strategies and their parameters are coordinated by the NILM in software as Joule modules, as described in Section III-B. All the experimental data were taken from equipment on USCGCs MARLIN, THUNDER BAY, and SPENCER, or equipment similar to that found on these ships. Vibration data were captured using Wilcoxon's model 728T single-axis 500-mV/g accelerometer [35].

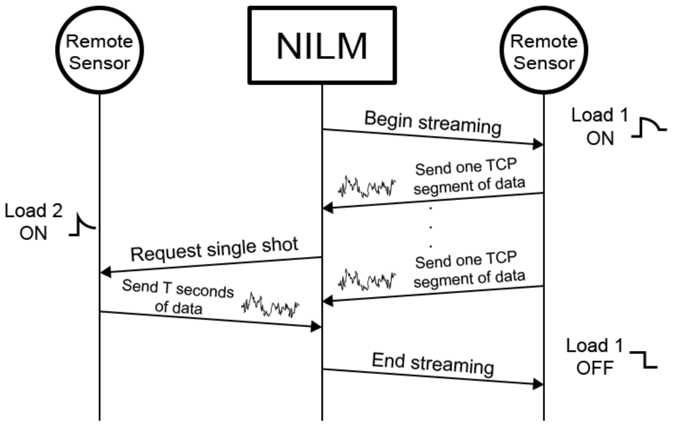

Fig. 12. FDD strategies described in Sections IV-A and IV-B.

The four FDD strategies are essentially: 1) continuously requesting remote sensor data for a load when the NILM detects that the load is running; 2) requesting only a small amount of remote sensor data for a load when the NILM detects that it turned on; 3) periodically requesting remote sensor data at a user-defined interval; and 4) continuously sending remote sensor data to the NILM whenever the remote sensor detects load operation. The first two strategies are useful for loads monitored by the NILM that turn on and off frequently. The third strategy is useful for loads that are almost always energized, since turn-on and -off events are not frequent enough to trigger sufficient data collection. The fourth strategy is useful for loads that are either not monitored by the NILM or have turn-on transients that are difficult or impossible to identify in the power stream.

A. Bilge and Fire Pump

The most straightforward FDD network strategy involves using the NILM to track the operational state of a load outfitted with a remote sensor, as illustrated in Fig. 12 (right). When the load is operating, the NILM continuously requests and downloads data from the remote sensor. The bilge and fire pump on USCGC MARLIN serves as an example of a fault for which this strategy is suitable. This centrifugal pump is designed to expel water from the bilge of the ship and supply water to the on-board firefighting system. The pump is driven by a three-phase induction motor that is rated to operate at 57.4 rps. In the stable and normal region of operation, the slope of the induction motor steady-state torque–speed curve is negative. The torque developed by the motor and consequently the power consumed increase when the rotor

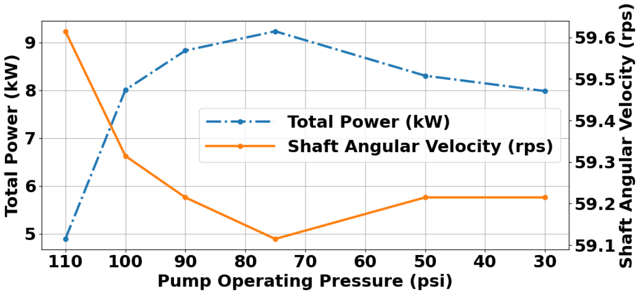

Fig. 13. Estimated power and shaft angular velocity for different operating pressures of the MARLIN bilge and fire pump.

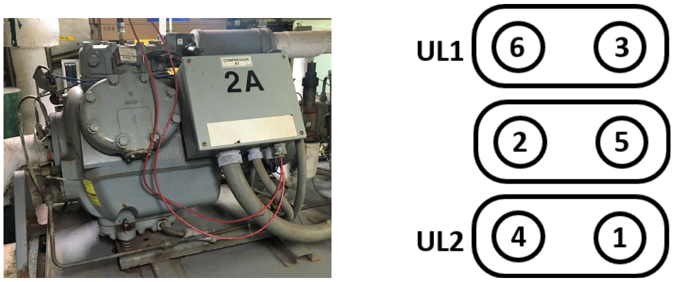

(a) (b)

Fig. 14. A/C compressor and unloader arrangement onboard SPENCER. (a) A/C compressor. (b) Piston and unloader arrangement.

speed decreases. Power can therefore provide an indicator of shaft speed. Measurement of the shaft speed is also possible from vibration measurements [36]. Under normal operation, the pump maintains a discharge pressure of approximately 110 psi. Changes in operating pressure maintained by the pump could be indicative of a variety of faults such as a blockage in the system or pump impeller wear. Both power and vibration measurements reflect changes in operating pressure of this load, as illustrated by the experiments presented in this section. In these experiments, the flow was adjusted with a controllable valve to simulate an increased demand of system. As the valve was adjusted, the outlet pressure of the pump varied from 110 to 30 psi. Power consumption and vibration were recorded using the installed NILM and an accelerometer connected to the wireless sensor platform, respectively. The accelerometer was affixed to the pump housing in a perpendicular orientation to the drive shaft.

Fig. 13 shows a plot of both the steady-state power consumption as measured by the NILM and shaft angular velocity [calculated from the discrete Fourier transform (DFT) of vibration data] across decreasing operating pressures. The steady-state power increases as the pressure changes from 110 to 75 psi, and then begins to slightly decrease as the pressure changes from 75 to 30 psi. The angular velocity of the bilge and fire pump's motor shaft decreases as the operating pressure changes from 110 to 75 psi, and then slightly increases as the pressure changes from 75 to 30 psi. This type of behavior is typical of normal operation of a backward centrifugal pump [37]. Both the curves have an inflection point at an operating pressure of 75 psi. This inflection identifies the point of operation where the pump is imparting the greatest work on the fluid, in terms of flow rate and pressure. Using these relationship curves, a change in operating pressure of the pump could be identified by either power or vibration data. Since this load turns on infrequently and is critical to shipboard operation, the proposed FDD network strategy produces two correlated indicators of faulty pump operation. In a practical NILM application, gradual changes in steady-state power may be difficult to resolve. Thus, tracking the operating pressure from the power consumption alone may be prone to errors. In addition to confirming changes in operating pressure detected in the power stream, vibration data can identify operating pressure changes that were missed in the power stream. By fusing these two sensors, the NILM has access to a more complete diagnostic picture than power and vibration provide individually.

B. Air Conditioning Plant

Unlike the previous example, some loads require a minimal amount of remote sensor data to be collected for disaggregation and fault detection. For this FDD network strategy, the NILM requests a small window of data from the remote sensor whenever it detects a transient event of interest related to that load, as illustrated in Fig. 12 (left). To demonstrate this, consider the A/C plant on USCGC SPENCER, which consists of two refrigeration skids. Each skid contains two independent refrigeration loops with semihermetic compressors; one compressor is shown in Fig. 14(a). The system is charged with R-134a refrigerant and cools a closed-loop chilled water system that circulates throughout the vessel. Each compressor has three piston pairs. A conceptual diagram of the pistons is shown in Fig. 14(b). Solenoid-activated unloaders, referred to as UL1 and UL2, are installed on two of the piston pairs and allow for capacity control. The unloaders activate piston pairs based on cooling demand for efficient system operation [38]. The center piston pair does not have an unloader and is always activated. Activated pistons pull refrigerant through the suction ports and discharge compressed refrigerant to the high-pressure side of the system. In the following discussion, loaded operation refers to six activated pistons, partially loaded refers to four activated pistons, and unloaded refers to two activated pistons.

Fig. 15 presents a power stream of an A/C skid onboard SPENCER. The power stream depicts the turn-on event of a single compressor and subsequent loading events of the compressor. Upon startup, the compressor operates in an unloaded condition with only the center piston pair (2 and 5) activated. With an increase in loading, the real power consumption increases while reactive power remains nearly constant. As a result, loading the compressor increases the load's power factor. For instance, the step increase at approximately 2.5 min in Fig. 15 is a shift from unloaded to partially loaded operation, with the center and lower piston pairs (1, 2, 4, and 5) activated. The final step in real power is a shift from partially loaded to fully loaded operation, with all the piston pairs (1–6) activated. Table II presents the observed power factor in each loading state.

The A/C compressors are driven by grid-connected induction motors. The induction motor has four poles and a rated

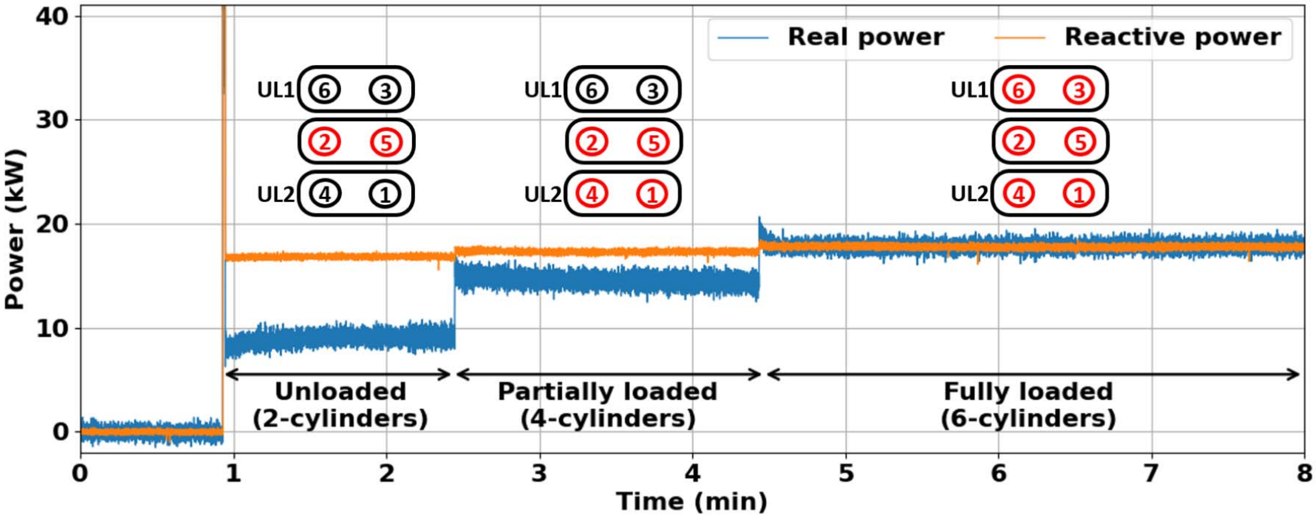

Fig. 15. SPENCER A/C compressor power stream.

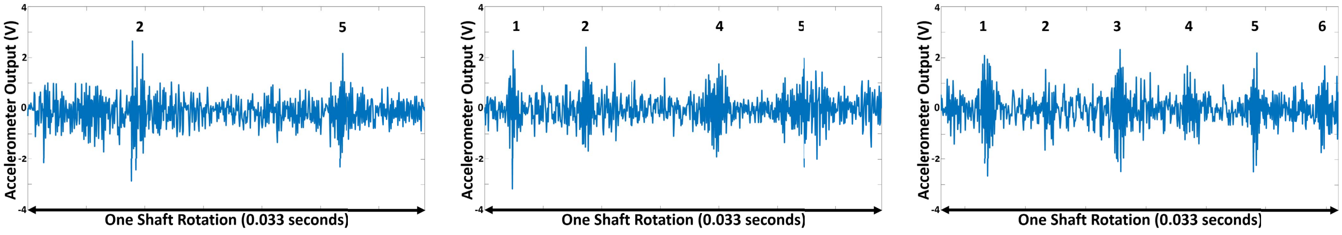

(a) (b) (c)

Fig. 16. SPENCER A/C compressor accelerometer time-domain plots of varying loading states. Impulsive events due to activated pistons are labeled. (a) Unloaded operation. (b) Partially loaded operation. (c) Loaded operation.

torque of 163 N·m while operating at 29.2 rps [39]. Fig. 16 shows the time-domain vibration measurements for each loading condition. Impulsive events due to activated pistons are evident in each case. Low-frequency content in the vibration signature is associated with mechanical events that occur throughout shaft rotation, such as crank and piston movement. Higher frequency content is likely a result of suction and discharge valve action, turbulent fluid flow, and excitation of natural structural frequencies of the compressor [40]. Vibration data were gathered using an accelerometer mounted to the discharge side of the compressor. At this location, measurements of 40 s in duration were taken at various loading conditions from eight compressors of the same model. In total, there were 32 loaded, 19 partially loaded, and 20 unloaded measurements. Based on the expected operating speed of 29.2 rps, the DFT is examined between 28.5 and 30 Hz. The location of the maximum value of the magnitude of the DFT in this range is an estimate of the shaft rotational frequency. The mean and standard deviation of the peak location for each loading condition are shown in Table II. This demonstrates that the compressor shaft rotational frequency is inversely related to loading.

TABLE II

A/C POWER FACTOR AND SHAFT FREQUENCY FOR LOADING CONDITIONS

Loading Condition	**Power Factor**	**Shaft Rotational Freq., Hz (σ_{Freq})**
2 cylinders	0.477	29.74 (0.0229)
4 cylinders	0.642	29.49 (0.0254)
6 cylinders	0.708	29.29 (0.0407)

If both the compressors on a skid are running, they will likely appear indistinguishable in the power stream. Thus, for healthy machines the NILM is unable to identify which compressor is responsible for a turn-on or loading transient. With access to the FDD network and one remote sensor, however, the NILM can track the loading condition of both the compressors. Upon observing a compressor loading event, the NILM requests a small sample of vibration data from the remote sensor deployed to one of the compressors (referred to as the "monitored compressor"). From this measurement, the NILM estimates the shaft rotational frequency and, from that, the loading condition of the monitored compressor. If this compressor's loading condition has not changed from what the NILM last observed, the NILM infers that the loading event occurred in the other compressor and updates that compressor's tracked state accordingly. Otherwise, the NILM updates the tracked state of the monitored compressor.

C. Crankcase Blower

In the third FDD network strategy, the NILM periodically requests data from the remote sensor at user-configured

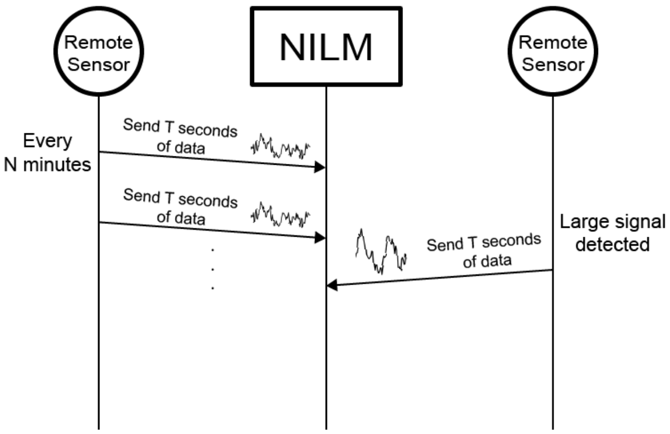

Fig. 17. FDD strategies described in Sections IV-C and IV-D.

TABLE III

CENTRIFUGAL FAN POWER AND VIBRATION COMPARISON

Operating Condition	Eccentric Mass, g	Apparent Power, VA (σ_{AP})	Norm. Rotational Freq. Magnitude
Normal	0	838.8 (1.757)	1.000
Imbalance 1	1.085	840.7 (1.858)	1.141
Imbalance 2	2.156	839.5 (1.662)	1.369
Imbalance 3	3.398	839.9 (1.728)	1.500

intervals, as illustrated in Fig. 17 (left). This strategy is motivated by imbalance condition faults, which are often invisible in the power stream but are apparent in vibration signatures. A controlled imbalance experiment using a centrifugal fan demonstrates this claim. Tests involved four conditions: a normal (balanced) condition and three imbalance conditions. The imbalance conditions were introduced with weights placed between blades of the fan's squirrel cage wheel. Ten power and vibration measurements of 30 s each were captured at each operating condition. The fan was operated at 19.2 rps for all the experiments. For each test, the average apparent power was computed over the 30-s measurement. Table III shows the average and standard deviation of these values for each condition. The magnitude of the DFT at the shaft rotational frequency is also shown, relative to the normal condition. The standard deviations of this frequency component were negligible. These results show that the operating condition did not change the apparent power. However, the magnitude of the DFT component at the shaft frequency and the operating condition are directly correlated. These results align with the findings presented in [41] and demonstrate a fault condition that is readily apparent in vibration measurements, but nearly impossible to diagnose in power measurements.

Similar findings were made onboard USCGC THUNDER BAY with its MPDE crankcase blowers. These centrifugal fans draw air from the engine's crankcase to prevent the buildup of combustible gases. The #1 MPDE's blower is shown in Fig. 18. Each blower is driven by an induction motor operating at 57.5 rps and acts to maintain a vacuum in the crankcase. The blowers are fitted with filters to remove atomized oil from the air drawn from the crankcase. The mounting arrangement creates an overhang condition, similar to a cantilever beam, for the induction motor and squirrel cage wheel. With this configuration, minor manufacturing defects, deterioration, or debris buildup on the fan blades can result in imbalance and excessive amounts of vibration. The blower's mounting arrangement is illustrated in Fig. 19(a). The mounting arrangement of the centrifugal fan used during the controlled imbalance experiment is shown in Fig. 19(b). Both create an overhang condition.

Fig. 18. THUNDER BAY MPDE crankcase blower.

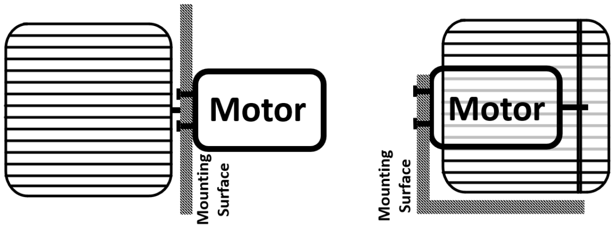

(a) (b)

Fig. 19. Cantilever mounting arrangements. (a) Crankcase blower mounting. (b) Centrifugal fan mounting.

The accelerometer measurements were first analyzed in the time domain and are shown in Fig. 20. It is apparent that there are significant differences in operation between the two blowers. The vibration signal envelope of the #1 blower is relatively uniform; the signal has an rms value of 0.596 V. The #2 blower displays a low-frequency oscillation at approximately 1.4 Hz and has an rms value of 0.278 V. Despite appearing drastically different, drawing firm conclusions from the time-domain observations alone is difficult. Variations in mounting, misalignment, bearing faults, and increased looseness of linkages can excite natural frequencies of a machine, affecting its vibration signal envelope [42]. Analysis of the vibration signals in the frequency domain provides more useful insight. The magnitudes of the first six orders in the frequency domain for both the blowers are shown in Fig. 21. The frequency content of the #1 blower is dominated by the first order. As shown during the controlled centrifugal fan experiment, this can indicate an imbalance condition in which an eccentric mass is oscillated once per shaft rotation [42]. The #1 blower is likely imbalanced due to an uneven buildup of soot and coagulated oil within the blower's rotating filter.

The steady-state apparent powers of the #1 and #2 blowers were approximately 646 and 786 VA, respectively. Without historical data, it is difficult to attribute the discrepancy in

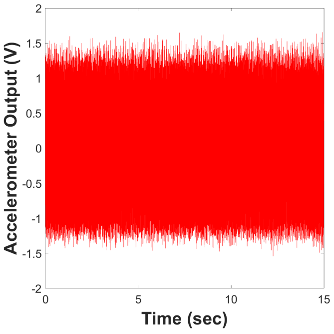

(a) (b)

Fig. 20. Crankcase blower time-domain comparison. (a) #1 Crankcase blower. (b) #2 Crankcase blower.

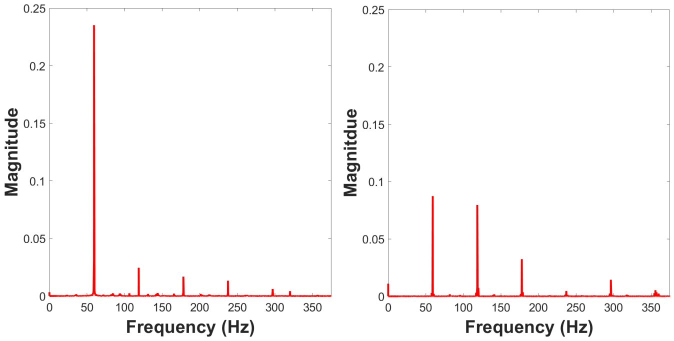

(a) (b)

Fig. 21. Crankcase blower frequency-domain comparison. (a) #1 Crankcase blower. (b) #2 Crankcase blower.

apparent power to a specific fault. Changes in power can be attributed to complex factors particular to the system, such as restrictions and leaks [37]. However, large first-order frequency content in vibration is a well-established indicator of imbalance [41], as corroborated by the controlled experiment. In practice, this type of load operates continuously, so turn-on and turn-off events will be sparse. With the proposed FDD network strategy, the NILM continually performs spectrum analysis on the periodically acquired vibration signals to generate diagnostics of imbalance conditions.

D. Sewage Vacuum Pumps

The final FDD network strategy presented addresses the case in which a load of interest does not draw power from a panel monitored by the NILM. For this strategy, the remote sensing device sends measurements to the NILM whenever it detects a signal exceeding a user-configured level, as illustrated in Fig. 17 (right). A pair of positive displacement vacuum pumps onboard USCGC THUNDER BAY provide a case study. These pumps maintain vacuum in the sewage collection tank and do not draw power from the panel monitored by the NILM on the ship. The vacuum sewage pumps operate in a lead-lag fashion, in which the primary pump turns on when vacuum in the collection tank drops below 12 inHg and the secondary pump turns on when vacuum drops below 10 inHg [43]. Once the collection tank vacuum reaches 18 inHg, both the pumps turn off and swap designations as primary and secondary pump, i.e., the primary pump becomes the secondary. These pumps are mounted on top of a small water tank that provides pump cooling and a fluid medium for the pumps to build vacuum via the Venturi effect.

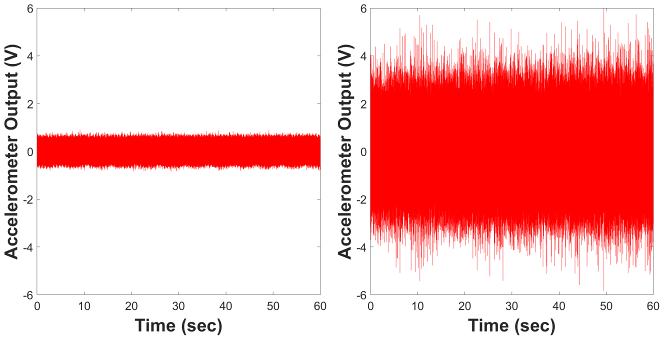

(a) (b)

Fig. 22. Vacuum pump time-domain comparison (prepair). (a) #1 Vacuum pump. (b) #2 Vacuum pump.

The wireless sensor platform captured vibration data from both the vacuum pumps using an accelerometer attached to each pump's motor housing. Fig. 22 shows the resulting time-domain measurements. The #2 pump exhibits a significantly higher rms value of vibration (1.013 V) than the #1 pump (0.306 V). Common fault diagnostic wisdom states that an increase in a machine's vibration level indicates deteriorated operation or a fault. Indeed, faults involving imbalances, mounting, or bearings can increase the vibration levels [42]. Without baseline measurements, one may be inclined to assume that the #2 pump is operating improperly since its vibration level is clearly larger than the #1 pump, which is supposed to be identical. The following demonstration of sophisticated signal processing techniques yields a surprising result: the #2 pump is healthy and #1 pump is the faulty one. By exploiting the cyclostationary nature of rotating machinery, these techniques offer this conclusion even without historical knowledge of the pump operating conditions.

Vibration measurements from rotating machinery are often modeled as realizations of cyclostationary random processes [34], [44], [45]. Cyclostationary random processes are characterized by periodic mean and autocorrelation functions [45]. Periodic vibrations of rotating machinery are due to shaft rotation, piston reciprocation, and other mechanical actions. In many systems, these periodic actions are associated with vibration content that is hard to model analytically such as friction, turbulent flow, and other physical factors. Vibrations from these phenomena are more broadband in frequency and are often modeled as random, with periodic actions modulating the random content. Cyclostationary signal processing tools provide important insights, for example, estimates of the spectral correlation function, or if normalized, the spectral coherence function. These estimates can quantify the frequency of the periodic actions and the nature of the modulation. The mean envelope spectrum (MES) is calculated from the spectral coherence function. Lines in the spectral coherence map at a specific cyclic frequency correspond to relative peaks in the MES and indicate cyclostationarity [22], [33].

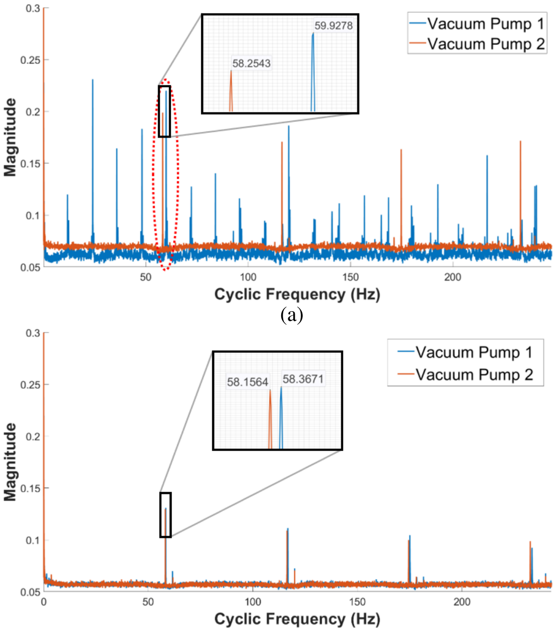

(a)

(b)

Fig. 23. Vacuum pump MES comparison. (a) Vacuum pump MES (prerepair). (b) Vacuum pump MES (postrepair).

Detailed mathematical discussions and intuitive examples of cyclostationary analysis are presented in [22] and [33]. Only the necessary definitions for the vacuum pump analysis are presented in this section. The spectral coherence function $\gamma_x^\alpha(f)$ is defined as

$$\gamma_x^\alpha(f) = \frac{\hat{S}_x^\alpha(f)}{\sqrt{\hat{S}_x^0\left(f-\frac{\alpha}{2}\right)\hat{S}_x^0\left(f+\frac{\alpha}{2}\right)}} \tag{1}$$

where $\hat{S}_x^\alpha(f)$ is the spectral correlation function for a signal x, f is the carrier or center frequency, and α is the cyclic frequency. For $\alpha = 0$, the spectral correlation function is equal to the traditional power spectral density (PSD). Equation (1) shows that the spectral coherence is the spectral correlation function normalized by a function of values from the PSD. The MES $S_x^{<f>}(\alpha)$ over some range of carrier frequencies F is defined as

$$S_x^{<f>}(\alpha) = \frac{1}{|F|}\int_F |\gamma_x^\alpha(f)|df \tag{2}$$

where F is chosen by the analyst and the upper bound of F is limited to one half of the sampling frequency (Nyquist frequency) [45]. Equation (2) defines the relationship between the spectral coherence and the MES.

In the case of the sewage pump, shaft rotation is the main periodic action that modulates broadband content. The vacuum pump motors are rated to operate at 57.5 rps. Thus, relative peaks in the MES at cyclic frequencies around 57.5 Hz and its integer multiples are expected. Fig. 23(a) depicts the MES of both the vacuum pumps as initially encountered on THUNDER BAY. The MES of the #1 pump has peaks at many cyclic frequencies unrelated to a reasonable shaft rotational frequency. The MES of the #2 pump has expected peaks at multiples of 58.25 Hz. Typically, MES values at cyclic frequencies that correspond to machine physics dominate the MES. When comparable in size to peaks without direct physical explanation, there is little modulation of broadband content and the system is likely not operating as intended. In addition, for systems with negligible broadband frequency content, the normalization in (1) with small values of the PSD could give rise to artificially large values of the spectral coherence function. Abnormal operation of the #1 pump is further confirmed by investigation of the area around 59 rps circled in Fig. 23(a). The MES peak of the #1 pump is at a noticeably higher cyclic frequency of 59.93 Hz. The shaft rotational frequency is very close to synchronous speed. This indicates the motor operates at very low slip and corresponds to a small load torque.

Fig. 24. Deteriorated vacuum relief valve.

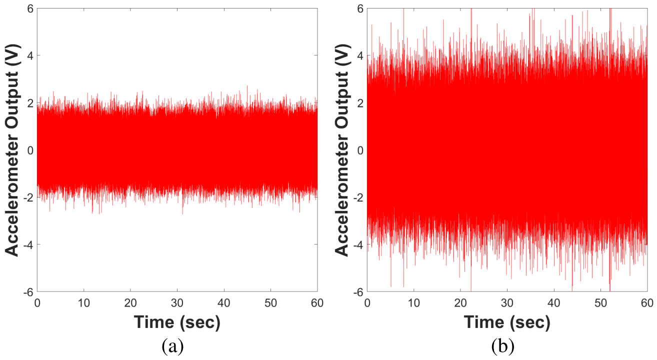

(a)

(b)

Fig. 25. Vacuum pump time-domain comparison (postrepair). (a) #1 Vacuum pump. (b) #2 Vacuum pump.

The differences in the MES prompted further examination of the system. Upon inspection, the #1 pump was not maintaining its water prime from the seal tank. Loss of prime causes the pump housing to become air-bound and deteriorates the pump's ability to build vacuum. The source of the fault was finally identified as the deteriorated sealing surfaces of the vacuum relief valve. Fig. 24 shows the deteriorated valve and its sealing surfaces.

Fig. 23(b) shows the MES profile from measurements taken after cleaning the sealing surfaces and reinstalling the valve. After repair, the MES of the two pumps is nearly identical and the additional MES peaks have vanished. The vibration of the #1 pump, as shown in Fig. 25, increased to an rms value of 0.571 V. Though the #1 pump's vibration level increased, it is still notably less than the #2 pump's rms value of 1.105 V. This may be the result of the differences in cumulative run time, mounting condition, or impeller health, but further inspection is required to confirm these suspicions.

This fault demonstrates that degraded operation can present counterintuitive time-domain vibration signatures. Without the aid of power stream data, cyclostationary vibration analysis successfully diagnosed the faulty relief valve. To integrate this diagnosis into the FDD network, the wireless sensor platform should alert the NILM when there is sufficient vibration to be of interest. Since MES calculation is computationally expensive, the sensor platform sends data either continuously or periodically to the NILM, which uses its higher computing power to perform MES analysis for fault detection.

V. CONCLUSION

Conventional nonintrusive power monitoring allows for energy management and fault diagnostics with a low sensor count. This work demonstrates that these abilities can be augmented with minimally invasive sensors to integrate auxiliary measurements. In facilitating online analysis, a local intranet of distributed sensors offers many of the benefits of the IoT model while avoiding the inherent security issues of using a public channel. Wireless networks provide advantages such as ease of setup and scalability. Wi-Fi testing and equipment diagnostics aboard ships show that this is a practical and flexible sensing solution for industrial sites. Four FDD network strategies for data acquisition are proposed, along with relevant case studies in condition monitoring.

ACKNOWLEDGMENT

The authors would like to thank the U.S. Coast Guard and the crews of USCGC MARLIN, USCGC SPENCER, and USCGC THUNDER BAY for access to their ships.

REFERENCES

[1] X. Wang, S. Lu, W. Huang, Q. Wang, S. Zhang, and M. Xia, "Efficient data reduction at the edge of industrial Internet of Things for PMSM bearing fault diagnosis," *IEEE Trans. Instrum. Meas.*, vol. 70, pp. 1–12, 2021.

[2] P. Ferrari, A. Flammini, E. Sisinni, S. Rinaldi, D. Brandão, and M. S. Rocha, "Delay estimation of industrial IoT applications based on messaging protocols," *IEEE Trans. Instrum. Meas.*, vol. 67, no. 9, pp. 2188–2199, Sep. 2018.

[3] G. Mois, T. Sanislav, and S. C. Folea, "A cyber-physical system for environmental monitoring," *IEEE Trans. Instrum. Meas.*, vol. 65, no. 6, pp. 1463–1471, Jun. 2016.

[4] T. A. Putra and J.-S. Leu, "Multilevel neural network for reducing expected inference time," *IEEE Access*, vol. 7, pp. 174129–174138, 2019.

[5] J. Paris, J. S. Donnal, and S. B. Leeb, "NilmDB: The non-intrusive load monitor database," *IEEE Trans. Smart Grid*, vol. 5, no. 5, pp. 2459–2467, Sep. 2014.

[6] D. H. Green, S. R. Shaw, P. Lindahl, T. J. Kane, J. S. Donnal, and S. B. Leeb, "A MultiScale framework for nonintrusive load identification," *IEEE Trans. Ind. Informat.*, vol. 16, no. 2, pp. 992–1002, Feb. 2020.

[7] R. Feng, W. Yuan, L. Ge, and S. Ji, "Nonintrusive load disaggregation for residential users based on alternating optimization and downsampling," *IEEE Trans. Instrum. Meas.*, vol. 70, pp. 1–12, 2021.

[8] S. Ghosh, A. Chatterjee, and D. Chatterjee, "An improved load feature extraction technique for smart Homes using fuzzy-based NILM," *IEEE Trans. Instrum. Meas.*, vol. 70, pp. 1–9, 2021.

[9] A. Aboulian et al., "NILM dashboard: A power system monitor for electromechanical equipment diagnostics," *IEEE Trans. Ind. Informat.*, vol. 15, no. 3, pp. 1405–1414, Mar. 2019.

[10] S. B. Leeb, P. Lindahl, D. Green, T. Kane, J. Donnal, and S. Kidwell, "Power as predictor and protector," *Soc. Nav. Architects Mar. Eng. (SNAME) Mar. Technol.*, pp. 28–35, Apr. 2019.

[11] J. Paris, J. S. Donnal, Z. Remscrim, S. B. Leeb, and S. R. Shaw, "The sinefit spectral envelope preprocessor," *IEEE Sensors J.*, vol. 14, no. 12, pp. 4385–4394, Dec. 2014.

[12] D. Green, T. Kane, S. Kidwell, P. Lindahl, J. Donnal, and S. Leeb, "NILM dashboard: Actionable feedback for condition-based maintenance," *IEEE Instrum. Meas. Mag.*, vol. 23, no. 5, pp. 3–10, Aug. 2020.

[13] P. A. Lindahl, D. H. Green, G. Bredariol, A. Aboulian, J. S. Donnal, and S. B. Leeb, "Shipboard fault detection through nonintrusive load monitoring: A case study," *IEEE Sensors J.*, vol. 18, no. 21, pp. 8986–8995, Nov. 2018.

[14] D. E. Phillips, R. Tan, M. Moazzami, G. Xing, J. Chen, and D. K. Y. Yau, "Supero: A sensor system for unsupervised residential power usage monitoring," in *Proc. IEEE Int. Conf. Pervasive Comput. Commun. (PerCom)*, Mar. 2013, pp. 66–75.

[15] Z. C. Taysi, M. A. Guvensan, and T. Melodia, "TinyEARS: Spying on house appliances with audio sensor nodes," in *Proc. 2nd ACM Workshop Embedded Sens. Syst. Energy-Efficiency Building*. New York, NY, USA: Association for Computing Machinery, 2010, pp. 31–36.

[16] A. Stief, J. R. Ottewill, J. Baranowski, and M. Orkisz, "A PCA and two-stage Bayesian sensor fusion approach for diagnosing electrical and mechanical faults in induction motors," *IEEE Trans. Ind. Electron.*, vol. 66, no. 12, pp. 9510–9520, Dec. 2019.

[17] B.-S. Yang and K. J. Kim, "Application of Dempster–Shafer theory in fault diagnosis of induction motors using vibration and current signals," *Mech. Syst. Signal Process.*, vol. 20, no. 2, pp. 403–420, Feb. 2006.

[18] B. Khaleghi, A. Khamis, F. O. Karray, and S. N. Razavi, "Multisensor data fusion: A review of the state-of-the-art," *Inf. Fusion*, vol. 14, no. 1, pp. 28–44, Jan. 2013.

[19] L. Jing, T. Wang, M. Zhao, and P. Wang, "An adaptive multi-sensor data fusion method based on deep convolutional neural networks for fault diagnosis of planetary gearbox," *Sensors*, vol. 17, no. 2, p. 414, Feb. 2017.

[20] H. Tian, "Dynamic pressure simulation of an external gear pump with relief chamber using a morphological approach," *IEEE Access*, vol. 6, pp. 77509–77518, 2018.

[21] M. Kulpa, "A vibrational study of gear pumps and gear pump drives," M.S. thesis, Rochester Inst. Technol., Rochester, NY, USA, 1991.

[22] L. Huchel, T. C. Krause, T. Lugowski, S. B. Leeb, and J. Helsen, "Chasing the cut: A measurement approach for machine tool condition monitoring," *IEEE Trans. Instrum. Meas.*, vol. 70, pp. 1–10, 2021.

[23] L. Huchel, T. C. Krause, S. B. Leeb, and J. Helsen, "Stretched sensing strategies for IEPE," *IEEE Trans. Instrum. Meas.*, vol. 70, pp. 1–10, 2021.

[24] S. Fong, J. Harmouche, S. Narasimhan, and J. Antoni, "Mean shift clustering-based analysis of nonstationary vibration signals for machinery diagnostics," *IEEE Trans. Instrum. Meas.*, vol. 69, no. 7, pp. 4056–4066, Jul. 2020.

[25] S. N. Diggavi, "On achievable performance of spatial diversity fading channels," *IEEE Trans. Inf. Theory*, vol. 47, no. 1, pp. 308–325, Jan. 2001.

[26] H. T. Friis, "A note on a simple transmission formula," *Proc. IRE*, vol. 34, no. 5, pp. 254–256, May 1946.

[27] M. Chen, K. Liu, J. Ma, and C. Liu, "Spatio-temporal fingerprint localization for shipboard wireless sensor networks," *IEEE Sensors J.*, vol. 18, no. 24, pp. 10125–10133, Dec. 2018.

[28] J. M. Batalla, "On analyzing video transmission over wireless WiFi and 5G C-band in harsh IIoT environments," *IEEE Access*, vol. 8, pp. 118534–118541, 2020.

[29] H. Farhat, H. Kdouh, C. Brousseau, G. Zaharia, G. Grunfelder, and G. El Zein, "Radio wave propagation characterization between adjacent decks on board ships," in *Proc. IEEE 82nd Veh. Technol. Conf. (VTC-Fall)*, Sep. 2015, pp. 1–4.

[30] X. Zeng, K. Liu, J. Ma, M. Chen, and M. Yu, "Reliability and delay trade-off analysis of unslotted IEEE 802.15.4 sensor network for shipboard environment," *IEEE Sensors J.*, vol. 21, no. 2, pp. 2400–2411, Jan. 2021.

[31] J. Donnal, "Joule: A real-time framework for decentralized sensor networks," *IEEE Internet Things J.*, vol. 5, no. 5, pp. 3615–3623, Oct. 2018.

[32] J. S. Donnal, "WattsWorth: An open-source platform for decentralized sensor networks," *IEEE Internet Things J.*, vol. 7, no. 1, pp. 189–196, Jan. 2020.

[33] L. Huchel, J. Helsen, P. A. Lindahl, and S. B. Leeb, "Diagnostics for periodically excited actuators," *IEEE Trans. Instrum. Meas.*, vol. 69, no. 7, pp. 4145–4153, Jul. 2020.

[34] J. Antoni, “Cyclostationarity by examples,” *Mech. Syst. Signal Process.*, vol. 23, no. 4, pp. 987–1036, May 2009.
[35] (2022). *Wilcoxon Research-Model 728T High Sensitivity, Low Noise Accelerometers*. [Online]. Available: https://buy.wilcoxon.com/
[36] C. Peeters et al., “Review and comparison of tacholess instantaneous speed estimation methods on experimental vibration data,” *Mech. Syst. Signal Process.*, vol. 129, pp. 407–436, Aug. 2019.
[37] J. W. O’Connell et al., “Nonintrusive ventilation system diagnostics,” *IEEE Sensors J.*, vol. 21, no. 17, pp. 19268–19278, Sep. 2021.
[38] *Technical Manual 3910A-514-A: Air Conditioning System*, United States Coast Guard, Washington, DC, USA, 2021.
[39] (2022). *Application Data-06D and 06E Semi-Hermetic Reciprocating Compressors*. [Online]. Available: https://www.shareddocs.com/hvac/docs/2002/Public/09/574-069.pdf
[40] J. N. Trout and J. R. Kolodzie, “Reciprocating compressor valve condition monitoring using image-based pattern recognition,” in *Proc. Annu. Conf. Prognostics Health Manag. Soc.*, 2016, pp. 1–10.
[41] G. Genta, *Dynamics of Rotating Systems*, 1st ed. Berlin, Germany: Springer, 2005.
[42] R. B. Randall, *Condition Based Monitoring-Industrial, Automotive, and Aerospace Applications*, 2nd ed. Hoboken, NJ, USA: Wiley, 2021.
[43] *Technical Drawing 101-WTGB-528–001: Sanitary and Deck Drains System Diagram*, United States Coast Guard, Washington, DC, USA, 2021.
[44] W. A. Gardner, *Statistical Spectral Analysis: A Nonprobabilistic Theory*. Englewood Cliffs, NJ, USA: Prentice-Hall, 1988.
[45] W. A. Gardner, *Introduction to Random Processes with Applications to Signals and Systems*. New York, NY, USA: Macmillan, 1986.

Aaron W. Langham (Graduate Student Member, IEEE) received the B.E.E. degree in electrical engineering from Auburn University, Auburn, AL, USA, in 2018, and the M.S. degree in electrical engineering and computer science from the Massachusetts Institute of Technology, Cambridge, MA, USA, in 2022, where he is currently pursuing the Ph.D. degree in electrical engineering and computer science.

His research interests include signal processing, machine learning, and computer systems for energy management.

Andrew Moeller received the M.S. degree in naval architecture and marine engineering from the Massachusetts Institute of Technology, Cambridge, MA, USA, in 2022.

He was previously stationed as the Damage Control Assistant onboard USCGC JAMES and as the Executive Officer onboard USCGC THUNDER BAY. He is currently a Lieutenant with the United States Coast Guard, stationed at Headquarters in Washington, DC, USA.

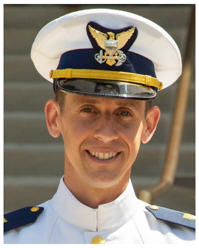

Devin W. Quinn received the M.S. degree in mechanical engineering from the Massachusetts Institute of Technology, Cambridge, MA, USA, in 2022.

He was previously stationed as a Damage Control Officer aboard USCGC DILIGENCE and Engineer Officer onboard USCGC ESCANABA. He is currently a Lieutenant Commander with the United States Coast Guard, Alameda, CA, USA.

Thomas C. Krause (Graduate Student Member, IEEE) received the B.S. degree in electrical engineering from Purdue University, West Lafayette, IN, USA, in 2019, and the M.S. degree in electrical engineering and computer science from the Massachusetts Institute of Technology, Cambridge, MA, USA, in 2021. He is currently pursuing the Ph.D. degree in electrical engineering and computer science with the Massachusetts Institute of Technology, Cambridge, MA, USA.

Daisy H. Green (Member, IEEE) received the B.S. degree in electrical engineering from the University of Hawai‘i at Mānoa, Honolulu, HI, USA, in 2015, and the M.S. and Ph.D. degrees in electrical engineering and computer science from the Massachusetts Institute of Technology (MIT), Cambridge, MA, USA, in 2018 and 2022, respectively.

She is currently a Post-Doctoral Associate with the Department of Architecture, MIT. Her research interests include signal processing for energy management and condition monitoring.

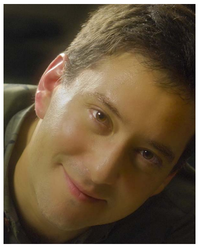

Steven B. Leeb (Fellow, IEEE) received the Ph.D. degree from the Massachusetts Institute of Technology, Cambridge, MA, USA, in 1993.

Since 1993, he has been a member on the faculty of the Department of Electrical Engineering and Computer Science, MIT, where he also holds a joint appointment with the Department of Mechanical Engineering. He is concerned with the development of signal processing algorithms for energy and real-time control applications.